

Room temperature high frequency transport of Dirac fermions in epitaxially grown Sb_2Te_3 based topological insulators

P. Olbrich¹, L. E. Golub², T. Herrmann¹, S. N. Danilov¹, H. Plank¹, V. V. Bel'kov², G. Mussler³, Ch. Weyrich³, C. M. Schneider³, J. Kampmeier³, D. Grützmacher³, L. Plucinski³, M. Eschbach³, and S. D. Ganichev¹

¹ Terahertz Center, University of Regensburg, 93040 Regensburg, Germany

² Ioffe Physical-Technical Institute, 194021 St. Petersburg, Russia and

³ Jülich Aachen Research Alliance (JARA-FIT), Leo Brandt Straße, 52425 Jülich, Germany

We report on the observation of photogalvanic effects in epitaxially grown Sb_2Te_3 three-dimensional (3D) topological insulators (TI). We show that asymmetric scattering of Dirac electrons driven back and forth by the terahertz electric field results in a *dc* electric current. Due to the “symmetry filtration” the *dc* current is generated in the surface electrons only and provides an opto-electronic access to probe the electric transport in TI, surface domains orientation and details of electron scattering even in 3D TI at room temperature where conventional surface electron transport is usually hindered by the high carrier density in the bulk.

A new state of matter called the topological insulator has recently been theoretically predicted and experimentally observed in a number of materials, such as Bi_2Se_3 , Sb_2Te_3 , and Bi_2Te_3 , for reviews see [1–3]. The main feature of TI emerges from its band structure. While the bulk of TI is an insulator with an inverted band structure its surface hosts gapless states with a linear energy dispersion. Thus, carriers at the surface of TI are expected to have unique properties, such as extremely high mobilities or a spin-locked transport behavior, and TI are considered to be prospective for novel applications in the field of spintronics, optoelectronics, or quantum computing. Hence, a fabrication of TI materials and, in particular, study of their transport properties moved into the focus of current research. However, in almost all known 3D TI the *dc* electron transport is often hindered by the high carrier density in the bulk [4–6]. A promising way to overcome this problem serves the recent progress in growth of 3D TI applying molecular-beam-epitaxy (MBE) technique, see e.g., [7, 8]. The existence of TI surface states in such materials has been demonstrated by the angle-resolved-photoemission-spectroscopy (ARPES) [9–11]. Furthermore, low-temperature electric measurements in thin films and nanowires indicate substantial surface state transport [12–18]. However, the electron transport exclusively determined by surface electrons, in particular, at room temperature, remains a challenge.

Here we report on the observation and study of a room temperature high frequency transport phenomena solely determined by 2D Dirac fermions in 3D TI. We show that excitation of MBE-grown Sb_2Te_3 crystals by terahertz (THz) electric fields results in a photogalvanic effects (PGE): a nonlinear transport effect yielding a *dc* electric current proportional to the square of the *ac* electric field [19, 20]. A selective excitation of *dc* current in TI surface states becomes possible due to the specific feature of PGE, whose prerequisite is a lack of inversion center. As Sb_2Te_3 crystals, like most of the 3D TI, is centrosymmetric, this requirement is fulfilled for the surface

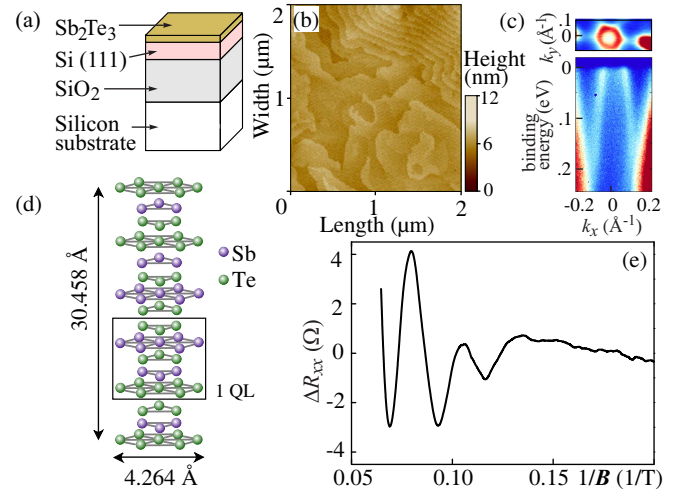


FIG. 1: (a) Sample sketch, (b) AFM surface scan (c) ARPES measurement showing *p*-type linear dispersion, (d) Structure of Sb_2Te_3 layer, and (e) SdH oscillations.

states only. Due to this “symmetry filtration”, the PGE is generated in the surface electron system only, even in the materials with substantial conductance in the bulk. We demonstrate that the PGE is caused by asymmetric scattering of Dirac electrons driven back and forth by the THz field. The effect reflects the surface symmetry and allows one to determine the orientation of the surface domains, to probe high frequency conductivity in TI, and to study tiny details of electron scattering.

Before discussing the experimental results we address the basic physics of the PGE in 3D TI and set requirements to the experimental geometry. The surface states of TI are based on the crystalline structure, see Fig. 1 (d), which includes a sequence of five atomic layers, so called a quintuple layer (QL), oriented perpendicularly to the *c*-axis [21]. The point group symmetry of Sb_2Te_3 bulk crystal is D_{3d} , which includes the center of inversion, whereas the *surface* lacks the space inversion and its point group is C_{3v} . The trigonal symmetry of 2D surface carriers makes

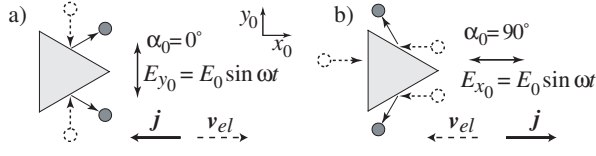


FIG. 2: Model of the PGE excited in Dirac fermions of Sb_2Te_3 TI due to asymmetry of elastic scattering by wedges.

the elastic scattering asymmetric giving rise to a *dc* electric current in response to *ac* electric field. The process of current generation is illustrated in Fig. 2 where the scatterers are sketched as randomly distributed but identically oriented wedges lying in the QL-plane. In the absence of radiation, the flows of anisotropically scattered electrons exactly compensate each other. Application of the linearly polarized THz field results in *alignment* of electron momenta: the total number of Dirac electrons driven back and forth by *ac* electric field $\mathbf{E}(t)$ increases while the number of particles moving, e.g. perpendicularly to the field direction, decreases. The corresponding stationary correction to the electron distribution function scales as a square of the *ac* electric field magnitude [22]. The alignment of electron momenta itself does not lead to the *dc* electric current but, due to asymmetric scattering by wedges, the excess of the number of carriers moving along the field violates the balance of the flows [23–25], and the linear PGE current is generated. The resulting current direction depends on the relative orientation of the *ac* electric field and wedges: e.g. the field parallel to the wedges base, see Fig. 2 (a), yields the current flowing in x_0 -direction while rotation of the electric field by 90° reverses the direction of the current, see Fig. 2 (b). Symmetry analysis yields the polarization dependence of the PGE current density \mathbf{j} :

$$\begin{aligned} j_{x_0} &= \chi(|E_{x_0}|^2 - |E_{y_0}|^2) = -\chi|E_0|^2 \cos 2\alpha_0, \\ j_{y_0} &= -\chi(E_{x_0}E_{y_0}^* + E_{y_0}E_{x_0}^*) = \chi|E_0|^2 \sin 2\alpha_0. \end{aligned} \quad (1)$$

Here E_0 is the electric field amplitude, the factor χ is the single linearly-independent constant, and α_0 is counted anti-clockwise from y_0 . Note that the brackets in the first and the second equations divided by $|E_0|^2$ represent the Stokes parameters [26] of the linearly-polarized radiation s_1 and s_2 , respectively.

In the bulk centrosymmetric Sb_2Te_3 crystals spatial inversion forbids the linear coupling between the current and electric field square and, in contrast to the surface, the PGE *dc* current cannot be generated. This difference has been addressed in Ref. [27], where control over TI photocurrents with light polarization was demonstrated by study of photon helicity-induced (circular) PGE. However, the strict “symmetry filtration” is violated due to a possible competing contribution of the photon drag effect [19, 20] which does not require the lack of inversion symmetry. While in analysis of Ref. [27] the photon drag

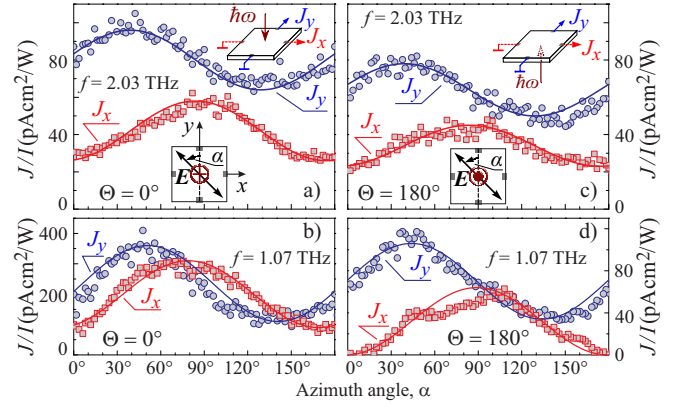


FIG. 3: Normalized photocurrents J_x/I and J_y/I for front (left panels) and back (right panels) illumination of the Sb_2Te_3 sample at room temperature. Solid lines show fits after Eqs. (3). Insets sketch the setups.

effect in the bulk has been ruled out due to its spin-degeneracy most recent observations demonstrated that substantial linear and circular photon drag currents can be efficiently generated even in 2D material with vanishing spin-orbit coupling, such as graphene, and gives a response comparable with PGE [19, 20, 28]. A straightforward way to distinguish the PGE response emerging from the surface states and photon drag effect provides experiments with reversed direction of the light propagation. Indeed while the PGE is determined by the electric field orientation and is insensitive to the radiation propagation direction the photon drag current being proportional to the photon momentum \mathbf{q}

$$j_{x_0} = \mathcal{T}|E_0|^2 q_z s_1, \quad j_{y_0} = -\mathcal{T}|E_0|^2 q_z s_2, \quad (2)$$

reverses its sign. Here \mathcal{T} is the photon drag constant and $z \parallel [111]$. Note that both types of the photocurrent behave identically upon variation of the radiation polarization state, cf. Eqs. (1) and (2). This indistinguishable behavior is also obtained for linear and circular photocurrents excited at oblique incidence, see Supplementary Material. The only way to separate the surface and the bulk transport is to excite photocurrents applying the radiation from both sides of the sample.

To explore the high frequency transport in Dirac fermion systems we studied photocurrents excited by THz radiation in Sb_2Te_3 grown by MBE on Si(111) wafers. A corresponding sketch of the structure is shown in Fig. 1 (a) and (d) and details of sample growth [8] are given in Supplementary Materials. At low temperatures ($T \approx 30$ K) the samples have a mobility of $290 \text{ cm}^2/\text{Vs}$ and *p*-type carrier density about $5 \times 10^{19} \text{ cm}^{-3}$. Values are obtained by standard transport measurements, see Fig. 1 (e) showing clear pronounced Shubnikov-de Haas (SdH) oscillations. The band gap E_g is in the order of 170 meV with the Fermi level referred to the Dirac point $\varepsilon_F \approx 65$ meV and a corresponding Fermi velocity,

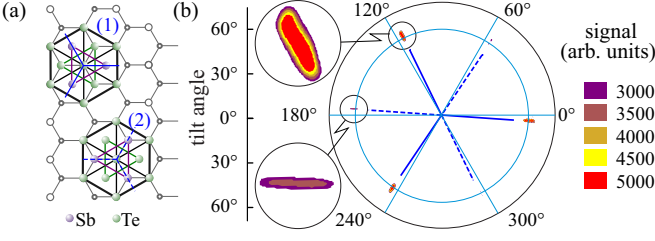


FIG. 4: (a) Two possible orientations of the domains. (b) Result of X-ray diffraction measurements on the Sb₂Te₃ sample, showing that one domain orientation dominates.

$v_0 = 4.36 \times 10^5$ m/s, measured by scanning tunneling spectroscopy and ARPES, see Fig. 1 (c). These results show that the sample should emerge topological properties, e.g. conducting surface states [8]. To measure current a pair of ohmic contacts ($R \approx 400 \Omega$) was centered on opposite edges of the squared shaped sample. To apply an ac electric field $\mathbf{E}(t)$ in the plane of QL we used a normally incident linearly polarized THz radiation of molecular laser [29–31], see insets in Fig. 3 and Supplementary Materials for details. The ac field direction was rotated by an azimuth angle α in respect to a sample edge defined as y -axis. The angle of incidence Θ for front and back illuminations were 0° and 180° , respectively.

Exciting Sb₂Te₃ samples with the THz electric field we observed a dc current exhibiting a characteristic polarization dependence shown in Fig. 3. Panels (a) and (b) present the photocurrents, $J_x(\alpha)$ and $J_y(\alpha)$, excited by front illumination and measured as a function of the ac electric field orientation. The signals are well fitted by

$$J_x = [-A(f) \cos(2\alpha - 3\Phi) + C(f)]I, \quad (3)$$

$$J_y = [A(f) \sin(2\alpha - 3\Phi) + C'(f)]I, \quad (4)$$

where A , C , C' and Φ are fitting parameters, and $I \propto E_0^2$ is the radiation intensity. The photocurrent for the back excitation ($\Theta = 180^\circ$) is shown in Fig. 3 (c) and (d). As an important result we obtained that the sign of the current as well as its dependence on the azimuth angle α remains unchanged. The same result is obtained for several other samples grown in the similar way (not shown). While in all samples the polarization dependence for front and back illumination remains unchanged the phase shift, being constant for each sample, varies from -4° to -10° .

Figure 3 shows that besides the offsets C and C' [32], the functional behavior of the photocurrents follows Eqs. (1) and (2) extended by a phase shift given by the angle 3Φ and using $\alpha = \alpha_0 + \Phi$, see Supplementary Material. The fact that the sign of the coefficient A remains unchanged at $\mathbf{q} \rightarrow -\mathbf{q}$ inversion unambiguously demonstrate that the photocurrent is dominated by the photogalvanic effect and, consequently, is generated in 2D Dirac fermions. Symmetry analysis of the photogalvanic effect shows that the 3Φ phase shift comes from the misorientation of y_0 -direction and the sample edge

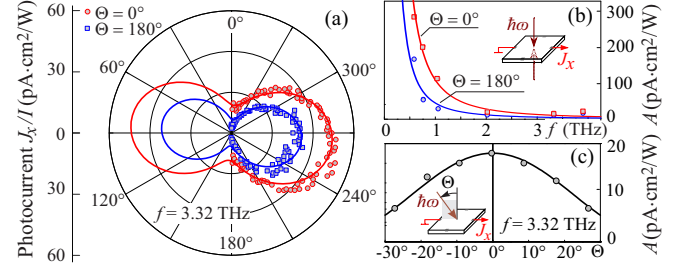


FIG. 5: (a) Photocurrents $J_x(\alpha)/I$ measured for front and back illumination at $T = 296$ K. Lines are fits after Eq. (3) with $\Phi = -4^\circ$. Coefficient A as a function of frequency f (b) and the angle Θ (c). Lines in (b) show fits after $A \propto 1/f^2$.

denoted as y axis, which in Eq. (1) is assumed to be zero. The phase shift 3Φ obtained for the arbitrary orientation wedges takes into account both the orientation of the ac electric field with respect to y_0 and the fact that the currents j_x and j_y are probed at angle Φ with respect to x_0 and y_0 , respectively. While being differently aligned with respect to the sample edges, all measurements reveal an almost uniform orientation of scattering centers characterized by the three-fold symmetry. The same result is obtained applying X-ray diffraction measurements. While two possible types of domains can be formed during the growth of Sb₂Te₃ on (111)-oriented Si substrate, see Fig. 4 (a), the X-ray data shown in Fig. 4 (b) demonstrate that the majority of the domains has the same orientation. As an important result, the angle $\Phi = -4^\circ$ obtained from the photocurrent measurements is equal to that measured by X-ray diffraction. This is clearly seen from comparison of Fig. 4 (b) and Fig. 5 (a), which shows the photocurrent $J_x(\alpha)/I = [-A(f) \cos(2\alpha + 12^\circ) + C]$ for front and back illumination in polar coordinates.

Varying the electric field frequency we obtained that the parameter $A(f)$, which determines the photocurrent magnitude, strongly increases with the frequency decrease. Figure 5 (c) shows that at low frequencies it closely follows the law $A \propto 1/f^2$. This figure also reveals that PGE for back irradiation is weaker than that for the front one. We attribute this result to either absorption in the substrate and/or to the contribution of PGE excited in the surface states at the SbTe/substrate interface, which can yield a different strength of the photoresponse of Dirac fermions.

Applying radiation at oblique incidence we found that the photocurrent given by the coefficients $A(f)$ slightly decreases with increasing the angle of incidence $|\Theta|$, see Fig. 5 (b). This fact indicates that in the described experimental arrangement the dominant contribution to the current stems from the PGE at normal incidence and other possible contributions of PGE or photon drag effect which, as addressed above, can be excited at oblique incidence do not play any substantial role. Additional experiments using circularly polarized light also revealed

that the circular photocurrent is either absent or hidden by the polarization independent photocurrent.

While the explanation of the photogalvanic effect has been given in a pictorial way above, we resort now to a microscopic description based on the Boltzmann kinetic equation for the electron distribution function $f_{\mathbf{p}}(t)$

$$\frac{\partial f_{\mathbf{p}}}{\partial t} + e\mathbf{E} \cdot \frac{\partial f_{\mathbf{p}}}{\partial \mathbf{p}} = - \sum_{\mathbf{p}'} (W_{\mathbf{p}',\mathbf{p}} f_{\mathbf{p}} - W_{\mathbf{p},\mathbf{p}'} f_{\mathbf{p}'}), \quad (5)$$

where the electric field $\mathbf{E}(t) = E_0 \exp(-i\omega t) + c.c.$, and $W_{\mathbf{p}',\mathbf{p}}$ is a probability for an electron to have the momenta \mathbf{p} and \mathbf{p}' before and after scattering, respectively. Lack of inversion center for the surface electrons makes their elastic scattering asymmetric: even for isotropic scatterers, $W_{\mathbf{p},\mathbf{p}'} \neq W_{-\mathbf{p},-\mathbf{p}'}$ [23, 24] and is given by

$$W_{\mathbf{p}',\mathbf{p}} = W_{\mathbf{p}',\mathbf{p}}^{(s)} + W_{\mathbf{p}',\mathbf{p}}^{(a)}, \quad (6)$$

where $W_{\mathbf{p}',\mathbf{p}}^{(s)} = W_{-\mathbf{p}',-\mathbf{p}}^{(s)}$ is the symmetric part, and the scattering asymmetry is described by $W_{\mathbf{p}',\mathbf{p}}^{(a)} = -W_{-\mathbf{p}',-\mathbf{p}}^{(a)}$. The absence of backscattering for Dirac fermions is taken into consideration by the standard factor in the symmetrical part [33]: $W_{\mathbf{p}',\mathbf{p}}^{(s)} \propto \cos^2[(\varphi_{\mathbf{p}'} - \varphi_{\mathbf{p}})/2]$, where $\varphi_{\mathbf{p}}, \varphi_{\mathbf{p}'}$ are the polar angles of the 2D vectors \mathbf{p} and \mathbf{p}' .

We iterate the kinetic equation in the second order in the field amplitude taking into account that $eE_0 v_0 \tau_{\text{tr}} / \varepsilon_F \ll 1$, where the linear 2D energy dispersion with the velocity v_0 is considered, and the transport scattering time, τ_{tr} , determining the mobility of 2D Dirac fermions is related to the symmetric part of the scattering probability as $\tau_{\text{tr}}^{-1} = \sum_{\mathbf{p}'} W_{\mathbf{p}',\mathbf{p}}^{(s)} [1 - \cos(\varphi_{\mathbf{p}'} - \varphi_{\mathbf{p}})]$. As a result, we find the stationary correction to the distribution function $\delta f_{\mathbf{p}} \propto |E_0|^2$ [22]. Calculating the photocurrent density by the standard expression $\mathbf{j} = e \sum_{\mathbf{p}} \delta f_{\mathbf{p}} v_0 \mathbf{p} / p$, we obtain

$$j_{x_0, y_0} = \pm s_{1,2} |E_0|^2 e v_0 \sigma(\omega) \times \left[\frac{1}{\varepsilon_F^2} \frac{d(\Xi \tau_2 \varepsilon_F^2)}{d\varepsilon_F} + \frac{1 - \omega^2 \tau_{\text{tr}} \tau_2}{1 + (\omega \tau_2)^2} \frac{\Xi \tau_2 \varepsilon_F}{\tau_{\text{tr}}} \frac{d(\tau_{\text{tr}} / \varepsilon_F)}{d\varepsilon_F} \right]. \quad (7)$$

Here the high-frequency conductivity is given by the Drude expression $\sigma(\omega) = n_s (e v_0)^2 \tau_{\text{tr}} / [\varepsilon_F (1 + \omega^2 \tau_{\text{tr}}^2)]$ with n_s being the concentration of 2D carriers which are degenerate, and $+s_1, -s_2$ correspond to j_{x_0}, j_{y_0} , respectively. The time τ_2 being of the order of τ_{tr} describes relaxation of the above discussed alignment of electron momenta. It is given by $\tau_2^{-1} = \sum_{\mathbf{p}'} W_{\mathbf{p}',\mathbf{p}}^{(s)} [1 - \cos 2(\varphi_{\mathbf{p}'} - \varphi_{\mathbf{p}})]$. The scattering asymmetry is taken into account by the factor $\Xi \ll 1$

$$\Xi = \tau_{\text{tr}} \sum_{\mathbf{p}'} \left\langle 2 \cos \varphi_{\mathbf{p}} \cos 2\varphi_{\mathbf{p}'} W_{\mathbf{p}',\mathbf{p}}^{(a)} \right\rangle_{\varphi_{\mathbf{p}}}, \quad (8)$$

where the brackets denote averaging over the directions of \mathbf{p} at the Fermi circle. Note that Eq. (7) agrees with Eqs. (1) obtained from the phenomenological arguments.

The microscopic theory of the PGE presented above describes all major features observed in the experiments. It shows that the *dc* electric currents probed along and normal to the wedges base are proportional to the square of the *ac* electric field amplitude $|E_0|^2$, described by one constant $A(f)I = \chi |E_0|^2$ and vary upon rotation of the electric field direction after the Stokes parameters s_1 and s_2 , respectively. Such a behavior is observed in the experiment, see Fig. 3. Then, the experimental data show that the photocurrent scales as $1/\omega^2$ at low frequencies, see Fig. 5 (b). This behavior follows from the theory: at $\omega \tau_{\text{tr}}, \omega \tau_2 \gg 1$ from Eq. (7) we obtain $j \sim e^3 v_0 \Xi |E_0|^2 / (\hbar^2 \omega^2)$. A small deviation from this behavior observed at high frequencies, see Fig. 5 (b), can be caused by the surface roughness, see Fig. 1 (b), which modifies the frequency behavior of $\sigma(\omega)$, like it has been reported for the epitaxial graphene [34] and other multilayer thin film systems, see e.g., [35]. Equation (7) also reveals that the magnitude of the PGE current, as well as its functional behavior upon variation of the electric field frequency or temperature, are determined by the dominant elastic scattering mechanism for Dirac fermions. In particular, the photocurrent can be generated for the scattering by Coulomb impurities or phonons but vanishes for that by short-range impurities, see Supplementary Materials. Thus, the observation of the PGE in Sb_2Te_3 crystals indicates the dominant role of the Coulomb scattering in the surface state electron transport. Furthermore, tiny details of scattering can be obtained from the study of the PGE spectral behavior at $\omega \tau_{\text{tr}} \leq 1$, where the scattering mechanism affects the frequency dependence of the photocurrent (via τ_{tr} and τ_2). Finally, we estimate the PGE magnitude following Eq. (7). We obtain for the radiation of $f = 0.6$ THz focused in 2.8 mm spot the experimental value $A = 280$ pA cm²/W for the scattering asymmetry factor $\Xi \sim 10^{-5}$. The latter value is consistent with the theoretical estimations, see Supplementary Materials.

To summarize, the observed photogalvanic effect in the surface states provides an opto-electronic method to selectively excite and study high frequency transport of the Dirac fermions in 3D TI. The photocurrent, being sensitive to the surface symmetry and scattering details, can be applied to map the domain orientation in 3D TI and study the high frequency conductivity of the surface states even at room temperature. Finally we note that while in the studied frequency range and materials the photoresponse is dominated by PGE our analysis demonstrates, that to ensure that the photoresponse comes from the Dirac fermions and to exclude a possible contribution of the bulk, the experiments with front and back sample excitation are required.

We thank M.M. Glazov, M. Schmalzbauer, E.L. Ivchenko and J.H. Bardarson for fruitful discussions. The support from the DFG (SPP 1666), HGF virtual Institute, RFBR and EU programme

POLAPHEN is gratefully acknowledged.

-
- [1] M. Z. Hasan and C. L. Kane, Rev. Mod. Phys. **82**, 3045 (2010).
- [2] J. E. Moore, Nature **464**, 194 (2010).
- [3] X. L. Qi and S. C. Zhang, Rev. Mod. Phys. **83**, 1057 (2011).
- [4] J. G. Checkelsky, Y. S. Hor, M. H. Liu, D. X. Qu, R. J. Cava, and N. P. Ong, Phys. Rev. Lett. **103**, 246601 (2009).
- [5] A. A. Taskin and Y. Ando, Phys. Rev. B **80**, 085303 (2009).
- [6] J. G. Analytis, J. H. Chu, Y. Chen, F. Corredor, R. D. McDonald, Z. X. Shen, and I. R. Fisher, Phys. Rev. B **81**, 205407 (2010).
- [7] S. Borisova, J. Krumrain, M. Luysberg, G. Mussler, and D. Grützmacher, Cryst. Growth Des. **12**, 6098(2012).
- [8] L. Plucinski, A. Herdt, S. Fahrenndorf, G. Bihlmayer, G. Mussler, S. Döring, J. Kampmeier, F. Matthes, D. E. Bürgler, D. Grützmacher, S. Blügel, and C. M. Schneider, J. Appl. Phys. **113**, 053706 (2013).
- [9] Y. L. Chen, J. G. Analytis, J. H. Chu, Z. K. Liu, S. K. Mo, X. L. Qi, H. J. Zhang, D. H. Lu, X. Dai, Z. Fang, S. C. Zhang, I. R. Fisher, Z. Hussain, and Z. X. Shen, Science **325**, 178 (2009).
- [10] Y. Xia, D. Qian, D. Hsieh, L. Wray, A. Pal, H. Lin, A. Bansil, D. Grauer, Y. S. Hor, R. J. Cava, and M. Z. Hasan, Nature Physics **5**, 398 (2009).
- [11] D. Hsieh, Y. Xia, D. Qian, L. Wray, J. H. Dil, F. Meier, J. Osterwalder, L. Patthey, J. G. Checkelsky, N. P. Ong, A. V. Fedorov, H. Lin, A. Bansil, D. Grauer, Y. S. Hor, R. J. Cava, and M. Z. Hasan, Nature (London) **460**, 1101 (2009).
- [12] J. Chen, H. J. Qin, F. Yang, J. Liu, T. Guan, F. M. Qu, G. H. Zhang, J. R. Shi, X. C. Xie, C. L. Yang, K. H. Wu, Y. Q. Li, and L. Lu, Phys. Rev. Lett. **105**, 176602 (2010).
- [13] K. Eto, Z. Ren, A. A. Taskin, K. Segawa, and Y. Ando, Phys. Rev. B **81**, 195309 (2010).
- [14] H. Steinberg, D. R. Gardner, Y. S. Lee, and P. Jarillo-Herrero, Nano Lett. **10**, 5032 (2010).
- [15] J. G. Analytis, R. D. McDonald, S. C. Riggs, J. H. Chu, G. S. Boebinger, and I. R. Fisher, Nature Physics **6**, 960 (2010).
- [16] L. B. Zhang, K. Chang, X. C. Xie, H. Buhmann, and L. W. Molenkamp, New J. Phys. **12**, 083058 (2010).
- [17] J. G. Checkelsky, Y. S. Hor, R. J. Cava, and N. P. Ong, Phys. Rev. Lett. **106**, 196801 (2011).
- [18] J. H. Bardarson and J. E. Moore, Rep. Prog. Phys. **76**, 056501 (2013).
- [19] E. L. Ivchenko, *Optical Spectroscopy of Semiconductor Nanostructures* (Alpha Science Int., Harrow, UK, 2005).
- [20] S. D. Ganichev and W. Prettl, *Intense Terahertz Excitation of Semiconductors* (Oxford Univ. Press, Oxford, 2006).
- [21] H. Zhang, C. X. Liu, X. L. Qi, X. Dai, Z. Fang, and S. C. Zhang, Nature Physics **5**, 438 (2009).
- [22] The stationary correction to the distribution function $f_p(t)$ is obtained by writing it as an expansion in powers of the electric field $f_p(t) = f_0 + f_p^{(1)}(t) + f_p^{(2)}$ with the oscillating in time term $f_p^{(1)}(t) \propto \exp(-i\omega t)$ and the stationary term $f_p^{(2)} \propto |E|^2$ being *second order* in the electric field.
- [23] V. I. Belinicher and B. I. Sturman, Sov. Phys. Usp. **23**, 199 (1980).
- [24] B. I. Sturman and V. M. Fridkin, *The Photovoltaic and Photorefractive Effects in Noncentrosymmetric Materials* (Gordon and Breach, Philadelphia, 1992).
- [25] W. Weber, L. E. Golub, S. N. Danilov, J. Karch, C. Reitmaier, B. Wittmann, V. V. Bel'kov, E. L. Ivchenko, Z. D. Kvon, N. Q. Vinh, A. F. G. van der Meer, B. Murdin, and S. D. Ganichev, Phys. Rev. B **77**, 245304 (2008).
- [26] M. Born and E. Wolf, *Principles of Optics* (Pergamon, Oxford, 1970).
- [27] J. W. McIver, D. Hsieh, H. Steinberg, P. Jarillo-Herrero, and N. Gedik, Nature Nanotech. **7**, 96 (2012).
- [28] M. M. Glazov and S. D. Ganichev, Phys. Reports **535**, 101 (2014).
- [29] J. Karch, P. Olbrich, M. Schmalzbauer, C. Zoth, C. Brinsteiner, M. Fehrenbacher, U. Wurstbauer, M. M. Glazov, S. A. Tarasenko, E. L. Ivchenko, D. Weiss, J. Eroms, and S. D. Ganichev, Phys. Rev. Lett. **97**, 227402 (2010).
- [30] S. D. Ganichev, E. L. Ivchenko and W. Prettl, Physica E **14**, 166 (2002).
- [31] E. Ziemann, S. D. Ganichev, I. N. Yassievich, V. I. Perel, and W. Prettl, J. Appl. Phys. **87**, 3843 (2000).
- [32] The polarization independent offset may be caused by the non perfectly flat surface, see the AFM photograph in Fig. 1, which locally reduces the symmetry of the surface states and allows a polarization independent contribution to the photogalvanic effect.
- [33] S. Das Sarma, S. Adam, E.H. Hwang, and E. Rossi, Rev. Mod. Phys. **83**, 407 (2011).
- [34] I. Crassee, M. Orlita, M. Potemski, A. L. Walter, M. Ostler, Th. Seyller, I. Gaponenko, J. Chen, and A. B. Kuzmenko, Nano Lett. **12**, 2470 (2012).
- [35] S. G. Engelbrecht, L. De Angelis, M. Toennies, and R. Kersting, Appl. Phys. A **113**, 641 (2013).

Supplementary material for “Room temperature high frequency transport of Dirac fermions in epitaxially grown Sb₂Te₃ based topological insulators”

P. Olbrich¹, L. E. Golub², T. Herrmann¹, S. N. Danilov¹, H. Plank¹, V. V. Bel’kov², G. Mussler³, Ch. Weyrich³, C. M. Schneider³, J. Kampmeier³, D. Grützmacher³, L. Plucinski³, M. Eschbach³, and S. D. Ganichev¹

¹ *Terahertz Center, University of Regensburg, 93040 Regensburg, Germany*

² *Ioffe Physical-Technical Institute, 194021 St. Petersburg, Russia and*

³ *Jülich Aachen Research Alliance (JARA-FIT), Leo Brandt Straße, 52425 Jülich, Germany*

SAMPLE PREPARATION

Our Sb₂Te₃ samples were grown by molecular beam epitaxy (MBE) on Si(111) wafers. Prior to the deposition, the Si substrates were chemically cleaned by the HF-last RCA procedure to remove the native oxide and passivate the surface with hydrogen. The substrates were subsequently heated in-situ to 600°C for 20 min to desorb the hydrogen atoms from the surface. The Sb and Te material fluxes were generated by effusion cells that were operated at temperatures of 450°C (Sb) and 380°C (Te). The Te shutter was opened 2 seconds before the Sb shutter, in order to saturate the Si substrate surface with Te. Throughout the growth, the substrate temperature was set at 300°C. A thickness of 27 nm Sb₂Te₃ were deposited at a slow growth rate of 9 nm/h in order to suppress domain formation and to obtain a smooth and uniform sample surface.

PHOTOCURRENT MEASUREMENTS

To excite photocurrent we used alternating electric field $\mathbf{E}(t)$ of terahertz radiation of TEA-CO₂ laser pumped terahertz molecular laser) [1–3]. The operating parameters of laser lines used in experiment are given in Table I. The applied single pulses had a duration of about 100 ns and repetition rate of 1 Hz. The radiation power was controlled by the THz photon drag detector [4]. The THz field was focused on a typical spot diameter of about 1 to 3 mm, being smaller than the sample size of 5×5 mm². The spatial beam distribution had an almost Gaussian profile which was measured by a pyroelectric camera [5]. The electric field amplitude of incoming radiation was varied from about 1 to 30 kV/cm (radiation intensities from ≈ 1 to 1000 kW/cm²). The *dc* current in response to terahertz electric field was measured in the unbiased samples by the voltage drop across a 50 Ω resistor. The signal was recorded with a storage oscilloscope. The initial laser radiation was linearly polarized along the *y*-axis. To vary the radiation polarization, $\lambda/2$ and $\lambda/4$ crystal quartz plates were employed. By applying the $\lambda/2$ plates, we varied the azimuth angle α between the polarization plane of the radiation incident upon the sample and the *y* axis. By applying $\lambda/4$ plates, we obtained elliptically (and circularly) polarized radiation. In this case, the polarization state is determined by the angle φ between the plate optical axis and the incoming laser polarization with electric field vector along the *y* axis. In particular, the radiation helicity

Table I: Characteristics of terahertz laser lines used in experiments.

<i>f</i> (THz)	λ (μ m)	$\hbar\omega$ (meV)	Line of CO ₂ Max. intensity		
			pump laser	(kW cm ⁻²)	Medium
8.57	35	35.3	10P(24)	300	NH ₃
3.95	76	16.3	10P(26)	10	NH ₃
3.32	90.5	13.7	9R(16)	1000	NH ₃
2.03	148	8.4	9P(36)	790	NH ₃
1.07	280	4.4	10R(8)	50	NH ₃
0.78	385	3.2	9R(22)	10	D ₂ O
0.61	496	2.5	9R(20)	8	CH ₃ F

is given by $P_{\text{circ}} = \sin 2\varphi$ [6].

PHOTO GALVANIC CURRENT IN THE ROTATED COORDINATE FRAME

The photogalvanic current direction is determined by the orientation of the electric vector in respect to crystallographic axes. Therefore, most convenient for this effect would be to investigate the current in the directions along and perpendicular to one of the mirror reflection planes of the C_{3v} point group. However, in real samples the direction of contacts may not coincide with the crystallographic axes. Therefore, we present here the equations describing photogalvanic current and its polarization dependence for the arbitrary orientation of contacts in respect to the crystallographic directions. To analyze this we introduce the angle Φ between the in-plane directions *x* and *y* along which the current is probed and the crystallographic axes *x*₀ and *y*₀, see Fig. 1. The symmetry consideration yields the expression for *x* and *y* components of the photogalvanic current excited at normal incidence:

$$\begin{aligned} j_x &= -\chi |E_0^2| \cos(2\alpha - 3\Phi), \\ j_y &= \chi |E_0^2| \sin(2\alpha - 3\Phi), \end{aligned} \quad (1)$$

where α is counted from *y*, i.e. $\mathbf{E}(\alpha = 0) \parallel \mathbf{y}$. For $\Phi = 0$ the azimuth angle $\alpha = \alpha_0$ and the above equation reduces to Eqs. (1) of the main manuscript. The phase shift 3Φ obtained for the arbitrary orientation wedges takes into

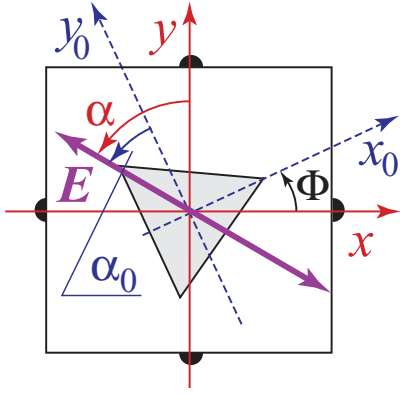


Figure 1: Schematic representation of the orientation of the crystallographic axes x_0, y_0 tilted by the angle Φ relative to the directions x, y along which the current is measured. Double arrow sketches the ac electric field vector \mathbf{E} . Azimuth angles α and α_0 are counted from the axes y and y_0 , respectively.

account both the orientation of the ac electric field with respect to y_0 and the fact that the currents j_x and j_y are probed at angle Φ with respect to x_0 and y_0 , respectively.

PHENOMENOLOGICAL THEORY OF PHOTOCURRENTS IN TI

While the paper is devoted to photogalvanic effect excited at normal incidence here, for completeness, we give the expressions for the photogalvanic and photon drag currents excited by oblique-incident radiation. We treat these nonlinear effects without going into microscopic details making use the symmetry arguments. This approach allows one to conclude on the experimental geometry and conditions of observation of the effect under consideration as well as to describe its variation with change of macroscopic parameters, such as intensity of the radiation, its polarization and angle of incidence without knowing of the microscopic origin. We consider the photocurrents generated in the surface states (point symmetry C_{3v}) and in the centrosymmetric bulk material (point group D_{3d}).

In the following we focus on the photocurrent contributions which can be generated at oblique incidence only. Note that the normal-incident radiation induced contributions of the PGE and photon drag effect described in the main text remain at oblique incidence. In general two kinds of the photocurrent can be generated at oblique-incident radiation

$$\mathbf{j}^{(oblique)} = \mathbf{j}^{(surf)} + \mathbf{j}^{(drag)}, \quad (2)$$

where $\mathbf{j}^{(surf)}$ caused by PGE in TI surface and $\mathbf{j}^{(drag)}$ is due to the photon drag effect where contributions from both surface and bulk are present which are phenomenologically identical in our system.

The photocurrent $\mathbf{j}^{(surf)}$ is a typical contribution for

any inversion-asymmetric two-dimensional system:

$$\begin{aligned} j_x^{(surf)} &= \chi_1(E_x E_z^* + E_z E_x^*) + \gamma P_{\text{circ}} |E_0|^2 \frac{q_y}{q}, \\ j_y^{(surf)} &= \chi_1(E_y E_z^* + E_z E_y^*) - \gamma P_{\text{circ}} |E_0|^2 \frac{q_x}{q}, \end{aligned} \quad (3)$$

where P_{circ} is the circular polarization degree given by $P_{\text{circ}} |E_0|^2 = i(\mathbf{E} \times \mathbf{E}^*) \cdot \mathbf{q}/q$. Here the constants χ_1 and γ describe the linear and circular PGE currents at oblique incidence which both are odd in the incidence angle Θ .

The photon drag effect induced photocurrent is a sum of two terms

$$\mathbf{j}^{(drag)} = \mathbf{j}^{(ax)} + \mathbf{j}^{(tr)}. \quad (4)$$

The contribution $\mathbf{j}^{(ax)}$ is independent of the microscopic details of the studied system and has the same form as in any uniaxial system [10]:

$$\begin{aligned} j_x^{(ax)} &= \tilde{T} P_{\text{circ}} |E_0|^2 \frac{q_y q_z}{q} + \mathcal{T}_1 q_x (|E_x|^2 + |E_y|^2) \\ &\quad + \mathcal{T}_2 [q_x (|E_x|^2 - |E_y|^2) + q_y (E_x E_y^* + E_y E_x^*)] \\ &\quad + \mathcal{T}_3 q_z (E_x E_z^* + E_z E_x^*) + \mathcal{T}_4 q_x |E_z|^2, \\ j_y^{(ax)} &= -\tilde{T} P_{\text{circ}} |E_0|^2 \frac{q_x q_z}{q} + \mathcal{T}_1 q_y (|E_x|^2 + |E_y|^2) \\ &\quad + \mathcal{T} [q_x (E_x E_y^* + E_y E_x^*) - q_y (|E_x|^2 - |E_y|^2)] \\ &\quad + \mathcal{T} q_z (E_y E_z^* + E_z E_y^*) + \mathcal{T} q_y |E_z|^2. \end{aligned} \quad (5)$$

Here \tilde{T} describes the circular photon drag current, and $\mathcal{T}_{1...4}$ are constants of the linear photon drag effect. Like $\mathbf{j}^{(surf)}$, the contribution $\mathbf{j}^{(ax)}$ is odd in the incidence angle Θ and at small Θ depends linearly.

The second kind of the photon drag photocurrents, $\mathbf{j}^{(tr)}$, is specific for trigonal systems and exists for both C_{3v} symmetry of the surface and D_{3d} symmetry of the bulk (in both cases the reflection plane is zx_0):

$$\begin{aligned} j_{x_0}^{(tr)} &= \mathcal{T} [q_{x_0} (E_{x_0} E_z^* + E_{x_0}^* E_z) - q_{y_0} (E_{y_0} E_z^* + E_{y_0}^* E_z)] \\ &\quad + \mathcal{T}' P_{\text{circ}} |E_0|^2 \frac{2q_{x_0} q_{y_0}}{q}, \end{aligned} \quad (6)$$

$$\begin{aligned} j_{y_0}^{(tr)} &= -\mathcal{T} [q_{y_0} (E_{x_0} E_z^* + E_{x_0}^* E_z) + q_{x_0} (E_{y_0} E_z^* + E_{y_0}^* E_z)] \\ &\quad + \mathcal{T}' P_{\text{circ}} |E_0|^2 \frac{q_{x_0}^2 - q_{y_0}^2}{q}, \end{aligned} \quad (7)$$

Note that, in contrast to $\mathbf{j}^{(surf)}$ and $\mathbf{j}^{(ax)}$, the trigonal contribution is an even function of the incidence angle: $j^{(tr)} \propto \Theta^2$ at small Θ .

DERIVATION OF THE PHOTOCURRENT

For derivation the expression for the photocurrent we solve the kinetic equation

$$\frac{\partial f_{\mathbf{p}}}{\partial t} + e\mathbf{E} \cdot \frac{\partial f_{\mathbf{p}}}{\partial \mathbf{p}} = - \sum_{\mathbf{p}'} (W_{\mathbf{p}', \mathbf{p}} f_{\mathbf{p}} - W_{\mathbf{p}, \mathbf{p}'} f_{\mathbf{p}'}), \quad (8)$$

up to the second order in the field \mathbf{E} and in the first order in $W_{\mathbf{p}',\mathbf{p}}^{(a)}$. We search the electron distribution function in the form $f_{\mathbf{p}}(t) = f_0(\varepsilon_p) + f_{\mathbf{p}}^{(1)}(t) + f_{\mathbf{p}}^{(2)}$ with the oscillating in time term $f_{\mathbf{p}}^{(1)}(t)$ and the stationary term $f_{\mathbf{p}}^{(2)} \propto |\mathbf{E}|^2$. The correction $f_{\mathbf{p}}^{(1)}$ is given by the standard expression

$$f_{\mathbf{p}}^{(1)} = -e\tau_{1\omega} f'_0 \mathbf{E} \cdot \mathbf{v}_{\mathbf{p}} + c.c., \quad (9)$$

where $f'_0 = df_0/d\varepsilon_p$, and we introduce complex relaxation rates $\tau_{n\omega}^{-1} = \tau_n^{-1} - i\omega$ with the elastic relaxation times ($n = 1, 2$) being

$$\frac{1}{\tau_n(\varepsilon_p)} = \sum_{\mathbf{p}'} W_{\mathbf{p}',\mathbf{p}}^{(s)} [1 - \cos n(\varphi_{\mathbf{p}'} - \varphi_{\mathbf{p}})]. \quad (10)$$

There are two contributions to $f_{\mathbf{p}}^{(2)}$. The first one is obtained by the following way: one first finds the quadratic in \mathbf{E} correction $\widetilde{f}_{\mathbf{p}}$ satisfying the equation

$$-i\omega \widetilde{f}_{\mathbf{p}} + e\mathbf{E} \cdot \frac{\partial f_{\mathbf{p}}^{(1)}}{\partial \mathbf{p}} = - \sum_{\mathbf{p}'} W_{\mathbf{p}',\mathbf{p}}^{(s)} (\widetilde{f}_{\mathbf{p}} - \widetilde{f}_{\mathbf{p}'}), \quad (11)$$

and then find $f_{\mathbf{p}}^{(2)}$ from the equation

$$\sum_{\mathbf{p}'} W_{\mathbf{p}',\mathbf{p}}^{(a)} \widetilde{f}_{\mathbf{p}'} + \frac{f_{\mathbf{p}}^{(2)}}{\tau_1} = 0. \quad (12)$$

Here we used the property $\sum_{\mathbf{p}'} W_{\mathbf{p}',\mathbf{p}}^{(a)} = 0$.

The second contribution is found by taking into account the scattering asymmetry and the second power of the field in the opposite way. In this approach, the oscillating \mathbf{E} -linear correction $\widetilde{f}_{\mathbf{p}}^{(1)}$ satisfies the equation

$$\sum_{\mathbf{p}'} W_{\mathbf{p}',\mathbf{p}}^{(a)} f_{\mathbf{p}'}^{(1)} + \frac{\widetilde{f}_{\mathbf{p}}^{(1)}}{\tau_{2\omega}} = 0, \quad (13)$$

and then the contribution $\delta f_{\mathbf{p}}^{(2)}$ is found from

$$e\mathbf{E} \cdot \frac{\partial \widetilde{f}_{\mathbf{p}}^{(1)}}{\partial \mathbf{p}} = - \frac{\delta f_{\mathbf{p}}^{(2)}}{\tau_1}. \quad (14)$$

Calculating the electric current by

$$\mathbf{j} = e \sum_{\mathbf{p}} \left(f_{\mathbf{p}}^{(2)} + \delta f_{\mathbf{p}}^{(2)} \right) \mathbf{v}_0 \frac{\mathbf{p}}{p}, \quad (15)$$

we obtain the result as a sum of two contributions corresponding to $f_{\mathbf{p}}^{(2)}$ and $\delta f_{\mathbf{p}}^{(2)}$, respectively:

$$j_x = |E_x|^2 \frac{N(ev_0)^3}{1 + (\omega\tau_{\text{tr}})^2} \times \left[\frac{\tau_{\text{tr}}}{\varepsilon_F^3} \frac{d(\Xi\tau_2\varepsilon_F^2)}{d\varepsilon_F} + \frac{1 - \omega^2\tau_{\text{tr}}\tau_2}{1 + (\omega\tau_2)^2} \Xi\tau_2 \frac{d(\tau_{\text{tr}}/\varepsilon_F)}{d\varepsilon_F} \right], \quad (16)$$

where $\tau_{\text{tr}} = \tau_1(\varepsilon_F)$, τ_2 also should be taken at $\varepsilon_p = \varepsilon_F$, and the factor Ξ is defined as

$$\Xi = \tau_{\text{tr}} \sum_{\mathbf{p}'} \left\langle 2 \cos \varphi_{\mathbf{p}} \cos 2\varphi_{\mathbf{p}'} W_{\mathbf{p}',\mathbf{p}}^{(a)} \right\rangle_{\varphi_{\mathbf{p}}}, \quad (17)$$

where the brackets denote averaging over the directions of \mathbf{p} at the Fermi circle.

ESTIMATION OF Ξ

The surface states in TI are formed in the Γ point from atomic z -orbitals which are odd and even in respect to the space inversion [7]. We denote the corresponding functions as Z_- and Z_+ , respectively, and the energy gap as E_g . The upper- and lower-lying bands are formed from odd (X_-, Y_-) and even (X_+, Y_+) x and y orbitals. For brevity, hereafter we assume that the Cartesian coordinates x, y coincide with the crystallographic axes x_0, y_0 . With account for the spin-orbit splitting, the Bloch functions in these bands in the Γ point are $(X_- + iY_-)/\sqrt{2}$ and $(X_+ - iY_+)/\sqrt{2}$. We denote the energy gaps between Z_+ and $(X_- + iY_-)/\sqrt{2}$ as E_{g1} , and between $(X_+ - iY_+)/\sqrt{2}$ and Z_- as E'_{g1} . In order to take into account mixing of the states at $p \neq 0$, we introduce the interband matrix elements of the momentum operator which are nonzero in the axial approximation:

$$P = \frac{i}{m_0} \langle Z_- | p_x | X_+ \rangle = \frac{i}{m_0} \langle Z_- | p_y | Y_+ \rangle, \quad (18)$$

$$P' = \frac{i}{m_0} \langle Z_+ | p_x | X_- \rangle = \frac{i}{m_0} \langle Z_+ | p_y | Y_- \rangle, \quad (19)$$

the matrix element which reflects the D_{3d} symmetry of the bulk crystal:

$$R = \frac{i}{m_0} \langle X_+ | p_y | Y_- \rangle = \frac{i}{m_0} \langle Y_+ | p_y | X_- \rangle \quad (20)$$

$$= \frac{i}{m_0} \langle Y_+ | p_x | Y_- \rangle = - \frac{i}{m_0} \langle X_+ | p_x | X_- \rangle,$$

and the matrix element accounting for the absence of $z \rightarrow -z$ reflection in surface:

$$V = \langle Z_+ | H_{\text{surf}} | Z_- \rangle. \quad (21)$$

Note that the values of V have opposite signs at two opposite (ideal) surfaces of the crystal.

Up to the second order in \mathbf{p} and the first order in V , the Bloch functions $Z_{\pm}(\mathbf{p})$ at a finite momentum \mathbf{p} have the following form:

$$Z_-(\mathbf{p}) = Z_- + \frac{1}{\sqrt{2}(E_g + E_{g1})} \quad (22)$$

$$\times \left[\frac{iVP'(p_x - ip_y)}{E_g} - \frac{RP(p_x + ip_y)^2}{E'_{g1}} \right] \frac{X_- + iY_-}{\sqrt{2}},$$

$$Z_+(\mathbf{p}) = Z_+ + \frac{1}{\sqrt{2}(E_g + E'_{g1})} \quad (23)$$

$$\times \left[\frac{iVP(p_x + ip_y)}{E_g} + \frac{RP'(p_x - ip_y)^2}{E_{g1}} \right] \frac{X_+ - iY_+}{\sqrt{2}}.$$

At $p \neq 0$, the surface states have the spinor wavefunctions being coherent superpositions of Z_- and Z_+ orbitals multiplied by the spin-up and spin-down spinors. Taking into account the \mathbf{p} -dependence of the Bloch amplitudes

Eqs. (22), (23) we obtain that the matrix element of elastic scattering by a potential $U(\mathbf{r})$

$$U_{\mathbf{p}'\mathbf{p}} = U_0(\mathbf{p}' - \mathbf{p}) \frac{\langle Z_-(\mathbf{p}') | Z_-(\mathbf{p}) \rangle + \langle Z_+(\mathbf{p}') | Z_+(\mathbf{p}) \rangle}{2}$$

contains the following term

$$U_{\mathbf{p}'\mathbf{p}} \propto U_0(\mathbf{p}' - \mathbf{p}) \left\{ 1 - i \frac{VRPP'}{4E_g} \times \left[\frac{(p_x + ip_y)^2(p'_x + ip'_y) - (p'_x - ip'_y)^2(p_x - ip_y)}{(E_g + E_{g1})^2 E'_{g1}} + \frac{(p_x - ip_y)^2(p'_x - ip'_y) - (p'_x + ip'_y)^2(p_x + ip_y)}{(E_g + E'_{g1})^2 E_{g1}} \right] \right\}. \quad (24)$$

Here $U_0(\mathbf{p}' - \mathbf{p})$ is the Fourier image of $U(\mathbf{r})$ multiplied by the factor $\cos[(\varphi_{\mathbf{p}'} - \varphi_{\mathbf{p}})/2]$. Note that a similar contribution can be obtained from admixture of $X_+ - iY_+$ to Z_- and $X_- + iY_-$ to Z_+ wavefunction by Vp^2 - and p -linear terms.

The presence of both real and imaginary terms in the scattering matrix elements leads to the scattering probability in the form

$$W_{\mathbf{p}',\mathbf{p}} = W_{\mathbf{p}',\mathbf{p}}^{(s)} + W_{\mathbf{p}',\mathbf{p}}^{(a)}, \quad (25)$$

where the symmetrical part is given by the standard expression

$$W_{\mathbf{p}',\mathbf{p}}^{(s)} = \frac{2\pi}{\hbar} \mathcal{N} \sum_{\mathbf{p}'} |U_0(\mathbf{p} - \mathbf{p}')|^2 \delta(\varepsilon_p - \varepsilon_{p'}) \quad (26)$$

with \mathcal{N} being a concentration of scatterers. The antisymmetrical part of the scattering probability is obtained in the third order in the scattering potential [8, 9]:

$$W_{\mathbf{p}\mathbf{p}'}^{(a)} = -\frac{2\pi}{\hbar} \mathcal{N} \delta(\varepsilon_p - \varepsilon_{p'}) \times 2\pi \sum_{\mathbf{p}_1} \text{Im} (U_{\mathbf{p}\mathbf{p}_1} U_{\mathbf{p}_1\mathbf{p}'} U_{\mathbf{p}'\mathbf{p}}) \delta(\varepsilon_p - \varepsilon_{p_1}). \quad (27)$$

This yields the following estimate

$$W_{\mathbf{p}\mathbf{p}'}^{(a)} \approx \frac{(2\pi)^2}{\hbar} \mathcal{N} \delta(\varepsilon_p - \varepsilon_{p'}) \frac{VRPP'p_F^3}{4E_g} \times \left[\frac{1}{(E_g + E_{g1})^2 E'_{g1}} + \frac{1}{(E_g + E'_{g1})^2 E_{g1}} \right] \times \sum_{\mathbf{p}_1} F(\varphi_{\mathbf{p}}, \varphi_{\mathbf{p}'}, \varphi_{\mathbf{p}_1}) \delta(\varepsilon_p - \varepsilon_{p_1}), \quad (28)$$

where

$$F(\varphi_{\mathbf{p}}, \varphi_{\mathbf{p}'}, \varphi_{\mathbf{p}_1}) = U_0(\mathbf{p} - \mathbf{p}_1) U_0(\mathbf{p}_1 - \mathbf{p}') U_0(\mathbf{p}' - \mathbf{p}) \times [\cos(2\varphi_{\mathbf{p}} + \varphi_{\mathbf{p}_1}) - \cos(2\varphi_{\mathbf{p}_1} + \varphi_{\mathbf{p}}) + \cos(2\varphi_{\mathbf{p}_1} + \varphi_{\mathbf{p}'}) - \cos(2\varphi_{\mathbf{p}'} + \varphi_{\mathbf{p}_1}) + \cos(2\varphi_{\mathbf{p}'} + \varphi_{\mathbf{p}}) - \cos(2\varphi_{\mathbf{p}} + \varphi_{\mathbf{p}'}).]$$

For short-range scattering potential $U_0(\mathbf{p}' - \mathbf{p}) = u \cos[(\varphi_{\mathbf{p}'} - \varphi_{\mathbf{p}})/2]$ with u being a constant we derive $\Xi = 0$, so the PGE current is not generated. This is a specific feature of Dirac fermions: for massive particles with a parabolic energy dispersion, $U_0(\mathbf{p}' - \mathbf{p})$ is independent of $\varphi_{\mathbf{p}'}$ and $\varphi_{\mathbf{p}}$ for short-range scattering, and PGE is present. For Coulomb impurity scattering, when $U_0(\mathbf{p}' - \mathbf{p}) \propto \cos[(\varphi_{\mathbf{p}'} - \varphi_{\mathbf{p}})/2]/|\sin[(\varphi_{\mathbf{p}'} - \varphi_{\mathbf{p}})/2]|$, Ξ is finite, i.e. PGE is present for Dirac fermions as well as for massive electrons.

We can estimate the factor Ξ defined in Eq. (17) as

$$\Xi \sim \frac{\varepsilon_F U_s}{(\hbar v_0)^2} \left(\frac{\varepsilon_F}{E_g} \right)^3 \frac{V}{E_g} \frac{RPP'}{v_0^3}, \quad (29)$$

where U_s is the characteristic energy of the scattering potential multiplied by its characteristic area. For $\varepsilon_F U_s / (\hbar v_0)^2 \sim 1$, $\varepsilon_F / E_g \sim 10^{-2}$, $V/E_g \sim 10^{-1}$, $P \sim P' \sim v_0$, and $R/v_0 \sim 10^{-2}$ we obtain $\Xi \sim 10^{-5}$. This value is consistent with the experimental results.

-
- [1] S. D. Ganichev and W. Prettl, *Intense Terahertz Excitation of Semiconductors* (Oxford Univ. Press, Oxford, 2006).
 - [2] P. Schneider, J. Kainz, S. D. Ganichev, V. V. Bel'kov, S. N. Danilov, M. M. Glazov, L. E. Golub, U. Roessler, W. Wegscheider, D. Weiss, D. Schuh, and W. Prettl, *J. Appl. Phys.* **96**, 420 (2004).
 - [3] J. Karch, P. Olbrich, M. Schmalzbauer, C. Zoth, C. Brinsteiner, M. Fehrenbacher, U. Wurstbauer, M. M. Glazov, S. A. Tarasenko, E. L. Ivchenko, D. Weiss, J. Eroms, and S. D. Ganichev, *Phys. Rev. Lett.* **97**, 227402 (2010).
 - [4] S. D. Ganichev, Y. V. Terent'ev, and I. D. Yaroshetskii *Pisma Zh. Tekh. Fiz.* **11**, 46 (1985) [*Sov. Tech. Phys. Lett.* **11**, 20 (1989)].
 - [5] E. Ziemann, S. D. Ganichev, I. N. Yassievich, V. I. Perel, and W. Prettl, *J. Appl. Phys.* **87**, 3843 (2000).
 - [6] S. D. Ganichev, E. L. Ivchenko and W. Prettl, *Physica E* **14**, 166 (2002).
 - [7] H. Zhang, C. X. Liu, X. L. Qi, X. Dai, Z. Fang, and S. C. Zhang, *Nature Physics* **5**, 438 (2009).
 - [8] V. I. Belinicher and B. I. Sturman, *Sov. Phys. Usp.* **23**, 199 (1980).
 - [9] B. I. Sturman and V. M. Fridkin, *The Photovoltaic and Photorefractive Effects in Noncentrosymmetric Materials* (Gordon and Breach, Philadelphia, 1992).
 - [10] M. M. Glazov and S. D. Ganichev, *Phys. Reports* **535**, 101 (2014) (2014).